Multiple-species model for electrokinetic instability

Michael H. Oddy[a] and Juan G. Santiago
Department of Mechanical Engineering, Stanford University, Stanford, California 94305

In this paper we present a multiple-species electrokinetic instability (MSEKI) model. We consider a high aspect ratio flow geometry, a base state where the conductivity gradient is orthogonal to the applied electric field (i.e., a spanwise gradient configuration), and a four-species chemistry model. A linear stability analysis (LSA) of the depth-averaged governing equations is shown to have unstable eigenmodes for conductivity ratios as close to unity as 1.01. We present the experimental image data and full nonlinear simulations of the governing equations for a conductivity ratio of 1.05. Images of the disturbance dye field from the nonlinear simulations show good qualitative agreement with the experiment. Both the trend and absolute value of the temporal evolution of the critical wave number are captured by the MSEKI model. Growth rates extracted from the experimental data also compare favorably with those predicted by LSA. Species electromigration is shown to have a significant influence on the development of the conductivity field and instability dynamics in multi-ion configurations. We anticipate this model to be of practical interest to researchers developing electrokinetically driven, chip-based bioanalytical devices. © *2005 American Institute of Physics*. [DOI: 10.1063/1.1931727]

I. INTRODUCTION

The past decade has witnessed a rapid advancement in the development of chip-based microfluidic devices commonly referred to as micro-total analysis systems.[1–4] Many of these devices apply electrokinetic liquid-phase, bioanalytical techniques including capillary electrophoresis and isoelectric focusing, and often manipulate samples having poorly characterized or unknown electrical conductivities. As a result, conductivity mismatches often occur between the sample/reagent species and the background electrolyte. Conductivity mismatches in the presence of applied electric fields can under certain conditions generate an unstable flow field. Although desirable for rapid-mixing applications, these instabilities are often unwanted in applications such as sample injection, separation, and controlled diffusion-limited reaction processes where it is desirable to minimize sample dispersion. This motivates research toward a better understanding of the conditions necessary for the onset of instability.

Instabilities occurring from the interaction of electric fields and conductivity gradients in so-called "leaky dielectric" liquid media have been observed since the 1960s.[5] Hoburg and Melcher published a seminal paper on electrohydrodynamic (EHD) instabilities observed for an electric potential applied transverse to a conductivity gradient in a flow cell which created an interface of ionically doped and undoped corn oil.[6] Their work showed that the interaction of an applied field and conductivity gradients generates regions of net charge in this low-conductivity (typically $10^{-7}-10^{-5}$ μS/cm) liquid system. Electric body forces imposed in liquid in these regions eventually lead to instability. Their model uses an unsteady conductivity transport equation that neglects conductivity transport by diffusion. As a result, their analysis showed their system to be unconditionally unstable for a wide range of investigated electric field strengths and conductivity ratios. It was later shown by Baygents and Baldessari that including the diffusive transport term in the conductivity equation resulted in a conditionally stable system, albeit they analyzed a configuration with an axial conductivity gradient.[7]

Since the first reported observation of electrokinetic instability (EKI) in an electrokinetic microsystem by Oddy *et al.* in 2001,[8] there has been renewed interest in the development of more accurate models for predicting threshold conditions for instability onset as well as other flow features including coherent wave structures and mixing rate. Chen *et al.* and Lin *et al.* showed that a generalized EHD modeling framework can be used to describe both low-conductivity, nondiffuse charge dynamics of classical EHD, and the more recently reported flow instabilities of high-conductivity electrolyte electrokinetic microsystems.[9,10] To date, models have used simple two-ion formulations consisting of a symmetric, binary electrolyte (SBE) to derive a transport equation for the conductivity, as part of a so-called Ohmic conduction model for ion transport.

Lin *et al.* analyzed the temporal stability properties of the two-ion SBE model, comprising the conductivity transport equation along with the conservation of momentum and electromigration current. They show that the model provides good qualitative and fair quantitative agreement with regard to the threshold electric field and critical wave number for a conductivity ratio $\gamma=10$. Lin *et al.* also presented nonlinear simulations of their set of governing equations that capture the high Peclet number stirring events observed in experiment. Chen *et al.* has shown the EKI to manifest itself convectively as well, which has lead to a linear stability analysis of the two-ion SBE model in a convective framework. In

[a]Electronic mail: oddy@stanford.edu

their analysis, the EKI is modeled using a linearized, thin-layer limit of the Navier–Stokes equations coupled with conservation equations for electrical conductivity and current. Their model reveals both convectively and absolutely unstable eigenmodes. More recently, Storey et al.[11] presented a depth-averaged version of the governing equations used by the Lin et al. model. Their depth-averaged model compared favorably with a complete three-dimensional model for thin channel geometries.

In this paper we present the following main contribution to the modeling of EKI and other complex electrokinetic flow systems. We relax the Ohmic conduction assumption, the core assumption of the SBE model, by considering a general multiple-species model that takes into account electromigration as a transport mechanism for conductivity. This general multi-ion model can be used to analyze either SBE or non-SBE systems. Here non-SBE systems refer to electrolytes consisting of either three or more ions or a binary ion system with asymmetric transport properties. For non-SBE systems, electromigration is shown to exert a potentially significant destabilizing or stabilizing mechanism depending on the initial ion configuration. The physical mechanism describing the role of electromigration in conductivity transport and flow stability is discussed.

Also presented here are a discussion and comparison of stiff versus nonstiff formulations of the governing equations, and the role of in-plane viscous stresses in a shallow channel modeled using depth-averaged equations. We present both linear stability analysis (LSA) and nonlinear simulation results for periodic boundary conditions applicable to our experiment and which show a temporal instability. At each step, we compare the new multiple-species electrokinetic instability (MSEKI) model with results from the simpler SBE model. We also discuss the influence of inertia in EKI and the assumption of electrokinetic slip versus stress-free boundary conditions at the walls bounding the spanwise dimension of the channel. We begin with a formulation of the governing equations in the following section.

II. THEORETICAL FORMULATION

Our aim in this section is to develop a set of scaled governing equations with appropriate boundary conditions. In Sec. IV, these equations will be used for performing a one-dimensional (1D) linear stability analysis and Sec. V presents a 2D nonlinear simulation of the equations. We begin with the equations of motion.

A. Dimensional balance laws

The flow field of an electrically conductive, incompressible liquid subject to an applied electric field $\mathbf{E}$ may be determined from the following conservation of mass and momentum equations:

$$\boldsymbol{\nabla} \cdot \mathbf{v} = 0, \tag{1}$$

$$\rho \frac{D\mathbf{v}}{Dt} = \rho\mathbf{g} + \boldsymbol{\nabla} \cdot (\mathbf{T}^m + \mathbf{T}^e), \tag{2}$$

where $\mathbf{v}$ and ρ represent the fluid velocity and density, respectively. $\mathbf{T}^m$ and $\mathbf{T}^e$ represent the mechanical and electrical stress tensors,[5,12,13]

$$T_{ij}^m = \mu\left(\frac{\partial v_i}{\partial x_j} + \frac{\partial v_j}{\partial x_i}\right) - \delta_{ij}p, \tag{3}$$

$$T_{ij}^e = \epsilon E_i E_j - \frac{1}{2}\epsilon\delta_{ij}E_k E_k, \tag{4}$$

where ϵ, p, and δ_{ij} represent the fluid permittivity, pressure, and Kronecker delta, respectively. Assuming constant viscosity μ, Eq. (2) may be expressed as

$$\rho \frac{D\mathbf{v}}{Dt} = -\boldsymbol{\nabla} p + \mu\nabla^2\mathbf{v} + \mathbf{f}_e, \tag{5}$$

where p represents the total pressure. The electrical forces arising from electrostriction are neglected in the analysis of this incompressible flow field.[13] $\mathbf{f}_e$ accounts for fluid stresses arising from free charge ρ_e and polarization due to gradients in permittivity, and may be written as

$$\mathbf{f}_e = \rho_e\mathbf{E} - \frac{1}{2}E^2\boldsymbol{\nabla}\epsilon. \tag{6}$$

For most electrokinetic instability analyses dealing with electrical conductivity gradients in the bulk, the electrical force due to polarization may be neglected relative to the electrical force associated with free or induced charge. However, here we include all terms for completeness.

Here in electrolyte systems of interest, dissociation of the solute generates ions resulting in free charge within the bulk.[14,15] The charge density is determined from summing the concentration distributions c_j associated with all ions present in the system:

$$\rho_e = F\sum_j z_j c_j. \tag{7}$$

Here F denotes Faraday's constant and z_j the valence number of the jth species. This charge distribution along with any externally applied electric potentials generate an electric field within the liquid that may be determined from Poisson's equation

$$\boldsymbol{\nabla} \cdot (\epsilon\mathbf{E}) = \rho_e. \tag{8}$$

Distributions of individual species concentrations may be determined from a species conservation equation of the form

$$\frac{Dc_j}{Dt} + \boldsymbol{\nabla} \cdot \mathbf{J}_{c_j} = 0, \tag{9}$$

where the molar flux $\mathbf{J}_{c_j}$ accounts for species transport due to electromigration (for charged species) and diffusion or

$$\mathbf{J}_{c_j} = F z_j \nu_j c_j\mathbf{E} - \kappa_j\boldsymbol{\nabla} c_j \tag{10}$$

κ_j and ν_j are, respectively, the molecular diffusivity and mobility of the jth species. In Eq. (9) we neglect species production resulting from chemical reactions. The molecular diffusivity may be related to the mobility through the Nernst–Einstein relation
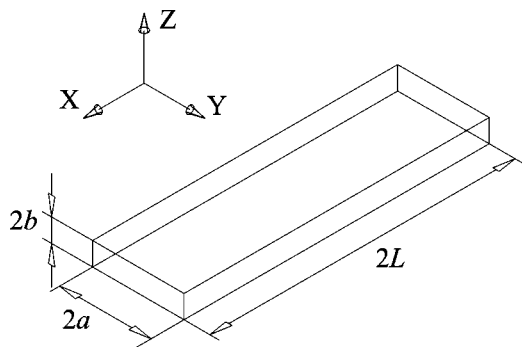
FIG. 1. Schematic of the rectangular cross-section microchannel geometry. The length of the channel is $2L$, while the spanwise and transverse directions are characterized by the width $2a$ and depth $2b$.

$$\kappa_j = RT\nu_j, \tag{11}$$

where R is the universal gas constant and T is the absolute temperature.

Finally, the electrical conductivity σ of the bulk liquid may be expressed in terms of the mobilities of the ions present or

$$\sigma = F^2 \sum_j z_j^2 \nu_j c_j. \tag{12}$$

It is convenient to express the conductivity in terms of molar conductivities Λ_j as

$$\sigma = \sum_j \Lambda_j c_j, \tag{13}$$

where $\Lambda_j = F^2 z_j^2 \nu_j$.

B. Scaling

The following reference scales are chosen to nondimensionalize the governing equations:

$$[x,y] = a, \quad [z] = b, \quad [u,v] = U_{\rm ev}, \quad [w] = \xi U_{\rm ev},$$

$$[t] = a/U_{\rm ev}, \quad [\phi] = E_o a, \quad [\rho_e] = \rho_{e,o} = \epsilon E_o/a,$$

$$[\sigma] = \sigma_o, \quad [p] = \epsilon E_o^2, \quad [c_j] = c_{j,o} = \sigma_o/\Lambda_j,$$

where the electroviscous velocity is $U_{\rm ev} = \epsilon E_o^2 a \xi^2/\mu$ and $\xi = b/a$ represents the depth to width aspect ratio. The channel geometry under consideration is shown in Fig. 1. E_o and σ_o denote the applied electric field (applied potential divided by $2L$) and mean conductivity at room temperature, respectively. For the remainder of this paper we shall assume that all material properties are uniform constants.

Using the reference scales listed above, the nondimensional mass and momentum conservation equations become

$$\nabla \cdot \mathbf{v} = 0, \tag{14}$$

$$\xi^2 \, {\rm Re} \frac{D\mathbf{u}}{Dt} = -\nabla_h p + \xi^2 \nabla_h^2 \mathbf{u} + \frac{\partial^2 \mathbf{u}}{\partial z^2} - \rho_e \nabla_h \phi, \tag{15}$$

$$\xi^4 \, {\rm Re} \frac{Dw}{Dt} = -\frac{\partial p}{\partial z} + \xi^4 \nabla_h^2 w + \xi^2 \frac{\partial^2 w}{\partial z^2} - \rho_e \frac{\partial \phi}{\partial z}, \tag{16}$$

where the Reynolds number is defined as ${\rm Re} = \rho U_{ev} a/\mu$ and $\mathbf{u} = \{u, v\}$. Since the electric field may be assumed to be irrotational, the electric field is represented as the gradient of a scalar potential or $\mathbf{E} = -\nabla \phi$. Poisson's equation and the expression for charge density scale as

$$\xi^2 \nabla_h^2 \phi + \frac{\partial^2 \phi}{\partial z^2} = -\xi^2 \rho_e, \tag{17}$$

$$\rho_e = \frac{F}{\rho_{e,o}} \sum_j c_{j,o} z_j c_j. \tag{18}$$

The nondimensional forms of the species conservation equations are

$$\xi^2 {\rm Pe}_j \frac{Dc_j}{Dt} = \xi^2 \nabla_h^2 c_j + \frac{\partial^2 c_j}{\partial z^2}$$
$$+ \chi_j \left[\xi^2 \nabla_h \cdot (c_j \nabla_h \phi) + \xi \frac{\partial}{\partial z}\left(c_j \frac{\partial \phi}{\partial z} \right) \right], \tag{19}$$

where ${\rm Pe}_j = U_{\rm ev} a/\kappa_j$ represents the diffusive Peclet number for the jth species. This scaling reveals another dimensionless parameter $\chi_j = (z_j e/kT_\infty) E_o a$. Physically, χ_j represents the ratio of the applied voltage to the thermal voltage of the bulk liquid associated with the diffusion of ions. Finally, the electrical and molar conductivity may be expressed in nondimensional form as

$$\sigma = \sum_j c_j. \tag{20}$$

The horizontal Laplacian operator in the xy plane is defined as $\nabla_h^2 \equiv (\partial^2/\partial x^2 + \partial^2/\partial y^2)$.

C. Asymptotic expansions and depth averaging

Assuming that each variable f may be expanded with respect to the aspect ratio ξ, as $f = f_o + \xi f_1 + \xi^2 f_2 + \cdots$, we may simplify the equation set to include only the leading order terms.[11] The resulting leading order terms are subsequently depth averaged using the operation $1/2 \int_{-1}^{1} f dz$ to eliminate the z dependence of the governing equations, yielding a set of two-dimensional equations.

We shall consider homogeneous Neumann boundary conditions for the transverse velocity, electric potential, and species concentration at the transverse boundary $z = \pm 1$;

$$\left. \frac{\partial w}{\partial z} \right|_{z=\pm 1} = 0, \tag{21}$$

$$\left. \frac{\partial \phi}{\partial z} \right|_{z=\pm 1} = 0, \tag{22}$$

$$\left. \frac{\partial c_j}{\partial z} \right|_{z=\pm 1} = 0. \tag{23}$$

Beginning with Poisson's and the species conservation equations, we observe that, to leading order, $\phi = \phi(x,y,t)$ and c_j

$=c_j(x,y,t)$, as a result of the no-flux boundary conditions at the channel walls. Consequently, to zeroth order the Poisson's and concentration equations become

$$\nabla_h^2 \phi = -\rho_e, \tag{24}$$

$$\text{Pe}_j \frac{D_h c_j}{Dt} = \nabla_h^2 c_j + \chi_j \nabla_h \cdot (c_j \nabla_h \phi), \tag{25}$$

where the material derivative in the xy plane is defined as $D_h f/Dt \equiv (\partial f/\partial t + \mathbf{u} \cdot \nabla_h f)$.

The leading order terms in the horizontal (xy plane) momentum equation are

$$\frac{\partial^2 \mathbf{u}}{\partial z^2} = \nabla_h p + \rho_e \nabla_h \phi. \tag{26}$$

From the transverse z-momentum equation, we observe that leading order pressure is independent of the z coordinate. Hence Eq. (26) may be directly integrated to yield

$$\mathbf{u} = -\frac{1}{3}(\nabla_h p + \rho_e \nabla_h \phi) + \mathbf{U}_{\text{eo}}, \tag{27}$$

where $\mathbf{U}_{\text{eo}} = -\nabla_h \phi / R_v$ represents the dimensionless electroosmotic velocity and $R_v = -\xi^2 E_o a/\zeta$ denotes the ratio of electroviscous to electroosmotic velocities. Equation (27) assumes that the ζ-potential is spatially uniform throughout the channel, a good approximation for the small conductivity ratios considered here.[16,17]

Using Eq. (27), the horizontal momentum equation may be rewritten as

$$\xi^2 \text{Re} \frac{D_h \mathbf{u}}{Dt} = -\nabla_h p + \xi^2 \nabla_h^2 \mathbf{u} - 3(\mathbf{u} - \mathbf{U}_{\text{eo}}) - \rho_e \nabla_h \phi. \tag{28}$$

We have chosen to retain the inertial and horizontal viscous stress terms for completeness. Since these terms are both of second order, the order of accuracy is not affected. In Sec. IV, we shall show that maintaining the horizontal viscous stress term plays an important role for damping high wave number disturbances. Finally, it can be shown from the transverse momentum equation, Eq. (16) with the boundary conditions given by Eq. (21), that the leading order transverse velocity component is $w=0$.

It is convenient to eliminate pressure from the momentum equations by switching from a primitive variables (u,v,p) approach to a vorticity/streamfunction (ω, ψ) formulation. Taking the curl of Eq. (28), we arrive at expressions for the fluid vorticity and streamfunction or

$$\xi^2 \text{Re} \frac{D_h \omega}{Dt} = \xi^2 \nabla_h^2 \omega - 3\omega - \nabla_h \rho_e \times \nabla_h \phi, \tag{29}$$

$$\nabla_h^2 \psi + \omega = 0. \tag{30}$$

Here the streamfunction ψ is related to the fluid velocity as

$$\mathbf{u} = \left\{ \frac{\partial \psi}{\partial y}, -\frac{\partial \psi}{\partial y} \right\}. \tag{31}$$

Lastly, a more detailed discussion on the asymptotic behavior of the SBE model is given by Lin *et al.*[18]

D. Depth-averaged equations and boundary conditions

In summary, the depth-averaged governing equations are shown below in nondimensional form,

$$\xi^2 \text{Re} \frac{D_h \omega}{Dt} = \xi^2 \nabla_h^2 \omega - 3\omega - \nabla_h \rho_e \times \nabla_h \phi, \tag{32}$$

$$\nabla_h^2 \psi + \omega = 0, \tag{33}$$

$$\text{Pe}_j \frac{D_h c_j}{Dt} = \nabla_h^2 c_j + \chi_j \nabla_h \cdot (c_j \nabla_h \phi), \tag{34}$$

$$\nabla_h^2 \phi = -\rho_e, \tag{35}$$

with the following definition for the nondimensional charge density:

$$\rho_e = \frac{F}{\rho_{e,o}} \sum_j c_{j,o} z_j c_j. \tag{36}$$

Equations (32)–(36) are solved in the domain Ω, subject to boundary conditions defined on $\Gamma = \partial\Omega$. Appropriate boundary conditions for the vorticity/streamfunction equations are of the form

$$\psi = g = -\int_{s_o}^s \mathbf{V}_\Gamma \cdot \mathbf{n} \, ds, \tag{37}$$

$$\frac{\partial \psi}{\partial n} = h = \mathbf{V}_\Gamma \cdot \mathbf{t}, \tag{38}$$

where $\mathbf{V}_\Gamma$ denotes the velocity on the domain boundary. Equation (37) is used to enforce a mass-flux condition through the domain boundary, while a no-slip or slip condition is enforced through Eq. (38). A stress-free condition may be used instead of Eq. (38) by enforcing a vorticity-free condition or $\omega = 0$. For Poisson's equation and the species concentration equations, the appropriate boundary conditions are of Robin form

$$\alpha_\phi \phi + \beta_\phi \nabla_h \phi \cdot \mathbf{n} = \varphi_\phi, \tag{39}$$

$$\alpha_{c_j} c_j + \beta_{c_j} \nabla_h c_j \cdot \mathbf{n} = \varphi_{c_j}. \tag{40}$$

For the remainder of this paper, we shall consider our system to be periodic in the axial or x direction. We therefore only need to enforce boundary conditions in the spanwise or y direction. For our system we considered either slip or stress-free conditions,

$$\left. \frac{\partial \psi}{\partial y} \right|_{y=\pm 1} = -\frac{1}{R_v} \left. \frac{\partial \phi}{\partial x} \right|_{y=\pm 1}, \tag{41}$$

$$\omega_{y=\pm 1} = 0. \tag{42}$$

The electrokinetic slip condition here is given by the electroosmotic velocity. To allow for a nonzero flow rate through the domain, and enforce no penetration, we set

$$\psi|_{y=-1} = 0, \tag{43}$$

$$\psi|_{y=+1} = g_+(t),\tag{44}$$

where $g_+(t)$ is given by

$$g_+(t) = \int_{-1}^{1} u_0(t)dy,\tag{45}$$

where u_0 denotes the zero-frequency component of the axial velocity u. We begin with the x component of the momentum equation, Eq. (28),

$$\xi^2 \, \mathrm{Re}\frac{D_h u}{Dt} = -\frac{\partial p}{\partial x} + \xi^2 \nabla_h^2 u - 3(u - U_{\mathrm{eo}}) - \rho_e \frac{\partial \phi}{\partial x}.\tag{46}$$

The zero-frequency mode is determined by the modified x-momentum equation

$$\xi^2 \, \mathrm{Re}\left(\frac{\partial u_0}{\partial t} + u \, \frac{\partial u}{\partial x}\bigg|_0 + v \, \frac{\partial u}{\partial y}\bigg|_0\right)$$
$$= \xi^2 \nabla_h^2 u_0 - 3(u_0 - U_{eo,0}) - \rho_e \, \frac{\partial \phi}{\partial x}\bigg|_0,\tag{47}$$

where the subscript "0" denotes the zero-frequency component. We note that $\partial p_0/\partial x = 0$, since there is no applied pressure gradient. If the electrokinetic slip condition, Eq. (41), is chosen, the appropriate boundary condition for Eq. (47) is

$$u_0|_{y=\pm 1} = -\frac{1}{R_v} \, \frac{\partial \phi_0}{\partial x}\bigg|_{y=\pm 1},\tag{48}$$

while for the stress-free condition, Eq. (42), the appropriate boundary condition is

$$\frac{\partial u_0}{\partial y}\bigg|_{y=\pm 1} = 0.\tag{49}$$

For the potential and concentration fields, homogeneous Neumann conditions are chosen:

$$\frac{\partial \phi}{\partial y}\bigg|_{y=\pm 1} = 0,\tag{50}$$

$$\frac{\partial c_j}{\partial y}\bigg|_{y=\pm 1} = 0.\tag{51}$$

With an appropriate set of initial conditions, this system is well posed. Despite the well posedness of the system, we have observed that this system is computationally "stiff." The stiffness of this system is due to the poor scaling of Poisson's equation and the definition of the charge density. In the following section we address this stiffness issue and derive a nonstiff formulation of the governing equations to mitigate computational difficulties associated with this stiff formulation of the governing equations.

E. Stiff versus nonstiff formulations

This stiffness may be observed by considering the following dimensionless form of Poisson's equation:

$$\nabla \cdot \mathbf{E} = \frac{F\Delta c_o a}{\epsilon E_o}\sum_j z_j c_j.\tag{52}$$

If we assume that the generated field is on the order of the applied field (for an applied field on the order of 10 kV/m), we discover that Δc_o is of $O(10^{-7} \text{ mol/m}^3)$. This suggests that relatively large gradients in the electric field may be generated by nanomolar concentration differences, giving rise to the "stiff" nature of this system. For the difficulties associated with the time advancement of numerically stiff equations, see, for example, Ref. 19. To circumvent this stiffness issue, the electric potential may under certain conditions be determined from a current continuity statement rather than directly from Poisson's equation. These conditions are discussed below.

A statement for current continuity may be derived by summing the species conservation equations for all j species resulting in a general charge conservation equation. The charge conservation equation in dimensional form is

$$\frac{D\rho_e}{Dt} + \nabla \cdot \mathbf{J}_{\rho_e} = 0,\tag{53}$$

where the charge density flux $\mathbf{J}_{\rho_e}$ is given as

$$\mathbf{J}_{\rho_e} = -\sum_j F^2 z_j^2 \nu_j c_j \nabla \phi - \sum_j F z_j \kappa_j \nabla c_j.\tag{54}$$

The first summation may be rewritten in terms of the more familiar bulk liquid electrical conductivity yielding

$$\mathbf{J}_{\rho_e} = -\sigma \nabla \phi - \sum_j F z_j \kappa_j \nabla c_j,\tag{55}$$

where the first term represents charge transport due to electromigration (conduction current) and the second due to molecular diffusion (diffusion current).

Equation (53) may be nondimensionalized as

$$\xi\frac{\epsilon U_{\mathrm{ev}}}{\sigma_o a}\frac{D\rho_e}{Dt} = \xi\nabla_h \cdot (\sigma\nabla_h\phi) - \frac{\partial}{\partial z}\left(\sigma\frac{\partial \phi}{\partial z}\right)$$
$$+ \sum_j \frac{1}{\chi_j}\left(\xi\nabla_h^2 c_j + \frac{1}{\xi}\frac{\partial^2 c_j}{\partial z^2}\right).\tag{56}$$

The leading order terms in this equation are

$$\frac{\epsilon U_{\mathrm{ev}}}{\sigma_o a}\frac{D\rho_e}{Dt} = \nabla_h \cdot (\sigma\nabla_h\phi) + \sum_j \frac{1}{\chi_j}\nabla_h^2 c_j.\tag{57}$$

The first nondimensional parameter $\epsilon U_{\mathrm{ev}}/\sigma_o a$ resulting from this scaling represents a ratio of the charge relaxation to advection time scale. For our parameter regime of interest this term is of the order of magnitude $O(10^{-5})$ at most and we shall therefore neglect it. The second parameter $1/\chi_j$ represents the ratio of diffusive to conductive current, which also appeared in the individual species conservation equations. The order of magnitude of this parameter is estimated to be $O(10^{-3})$. Despite the small order of magnitude of this term, the diffusive current becomes important for high wave number disturbances as will be shown in Sec. IV. We shall therefore retain this term. The charge conservation equation reduces to a current conservation equation of the form

$$\nabla_h \cdot (\sigma \nabla_h \phi) + \sum_j \frac{1}{\chi_j} \nabla_h^2 c_j = 0. \tag{58}$$

We will refer to Eqs. (32)–(36) as the stiff (S) set, while the same set of equations with Eqs. (20) and (58) substituted for Eq. (36) represents the nonstiff (Non-S) set. Finally we note for the Non-S set, Poisson's equation is only used to relate the charge density to the potential, while the potential itself is determined from the current continuity expression [Eq. (58)]. We also observe that while the charge density is small, assuming strict electroneutrality (i.e., zero charge density throughout) would be incorrect. The deviation from electroneutrality provides the source of coupling between the concentration, applied electric, and flow fields, ultimately resulting in the rich phenomena we observe.

III. CHEMISTRY MODEL

The electrolyte chemistry of our experiments warrants discussion. As mentioned above, the dissociation of solute molecules, typically salts or other strong electrolytes, produces free charge within the bulk solvent. It is very difficult to account for all sources of ions in our electrolyte (e.g., including impurity ions, buffer ions, and carbonic acid ions resulting from water and carbon dioxide reactions), so we shall consider only the major sources. The bulk electrical conductivity of our liquid was tailored using potassium chloride, while scalar flow visualization was accomplished by adding a dextran-rhodamine B conjugate (a sugar molecule chemically conjugated to a fluorescent molecule—see a description of the experimental setup below). We were interested in visualizing mass transport associated with fluid advection rather than molecular diffusion, so we chose a high-molecular weight (70 kDa) dextran-conjugated form of the rhodamine B fluorophore. While the rhodamine B dye molecule is expected to be net neutral due to its zwitterionic structure,[20] we observed that adding a 2 μM molar density of dextran-rhodamine B dye conjugate to the potassium chloride solution consistently resulted in a slight increase, on the order of 1 μS/cm, of the solution conductivity. After close consultation with the manufacturer, we conclude that this slight increase in ionic concentration is most likely a result of charged amine group(s) on the dextran molecule. We therefore chose a simplified four-ion model to represent this system. In this model, we assume that the ions in largest abundance result from the full dissociation of potassium chloride,

$$\text{KCl} \rightarrow \text{K}^+ + \text{Cl}^-. \tag{59}$$

Consistent with the experiment, K$^+$ and Cl$^-$ ions are assumed to be initially uniformly distributed throughout the field. Conductivity gradients in the field are due to the presence of the dextran-rhodamine B conjugate. We model the dextran-rhodamine B conjugate as a molecule AB which dissociates as follows:

$$AB \rightarrow A^+ + B^-. \tag{60}$$

We make the simplest assumption regarding A^+ and its counterion B^-, and assume that these form a symmetric, monova-

lent ion pair. Note that, although the KCl and AB solutes each form symmetric electrolyte pairs, the four-ion system considered here is strongly asymmetric (resulting in strong gradients in ion mobility). This is due to the significant difference in mobility and diffusivity of AB versus KCl ions, and is a reason for considering a four-ion model. We estimated the effective diffusivity of this pair from image data of the molecular diffusion of an initial sharp interface (in the absence of an electric field) and related diffusivity to mobility using the Nernst–Einstein relation. Diffusivity and mobility values are given in the experimental setup section below.

IV. LINEAR STABILITY ANALYSIS

In the experiment, the spanwise gradient is solely due to the presence of the dye-dextran conjugate ions. Although the resulting conductivity ratio is small (on the order of 1.05), a linear stability analysis suggests this slight gradient is in fact significant and can destabilize the flow and dominate mass transport. We present here a one-dimensional linear stability analysis on the S equation set and consider the case of a streamwise applied electric field and a spanwise conductivity gradient.

In accordance with standard linear stability analyses, we begin by expanding each unknown in terms of its base state and a perturbation of vanishing amplitude or $f(\mathbf{x}, t) = \bar{f}(\mathbf{x}, t) + f'(\mathbf{x}, t)$.[21] The resulting equations are subsequently linearized yielding a system of disturbance equations. We consider a steady base state with only spanwise variation and assume normal modes of the form $f(\mathbf{x}, t) = \bar{f}(y) + \hat{f}(y) \exp(ikx + st)$. Here the wave number k is a real variable, while the eigenvalue s is complex (i.e., $s = s_R + i s_I$, where i denotes the unit imaginary number). The real part of s, s_R, represents the growth rate and the phase speed of the disturbance is denoted by $-s_I/k$. The system is considered to be linearly unstable to infinitesimal disturbances for $s_R > 0$. The normal mode expansion leads to an algebraic eigenvalue problem that is solved for each k and range of the nondimensional parameters of interest.

For the base state, we considered the K$^+$ and Cl$^-$ ions to be uniformly distributed and the A^+ and B^- ions to have a distribution consistent with 95 s of diffusion time prior to the initiation of the electric field. This A^+ and B^- ion distribution was obtained using a simple one-dimensional diffusion simulation with the profiles of Fig. 2 as an initial condition. The initial 95 s period of diffusion is equal to the advection time of the liquid as it travels from the channel inlet to the viewing area of the experiment (5 s) plus an additional 90 s of diffusion prior to activation of the electric field. The final base-state distribution of A^+ and B^- ions is given by the solution of the following equation:

$$\text{Pe}_j \frac{\partial \bar{c}_j}{\partial t} = \frac{\partial^2 \bar{c}_j}{\partial y^2}, \tag{61}$$

subject to homogeneous Neumann boundary conditions $\partial \bar{c}_j / \partial y |_{y = \pm 1} = 0$. Note, we have neglected the electromigration terms here since the ion pairs are assumed to have equal diffusivities, so that a liquid junction potential is not expected to develop.[22] Moreover, the base-state applied electric
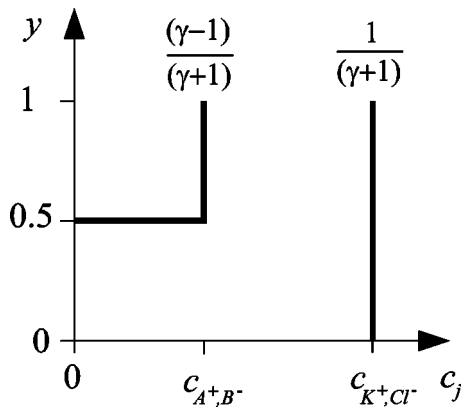
FIG. 2. Base-state concentration profiles of four-ion model. At the start of the process, the concentration of KCl ions is uniform. The initial distribution of A^+ and B^- ions is the end-state of a simple 95 s diffusion of the initial Heaviside distribution. This preliminary diffusion of the boundary results in an interface width of $\approx 410\ \mu$m for the A^+ and B^- concentration distributions.
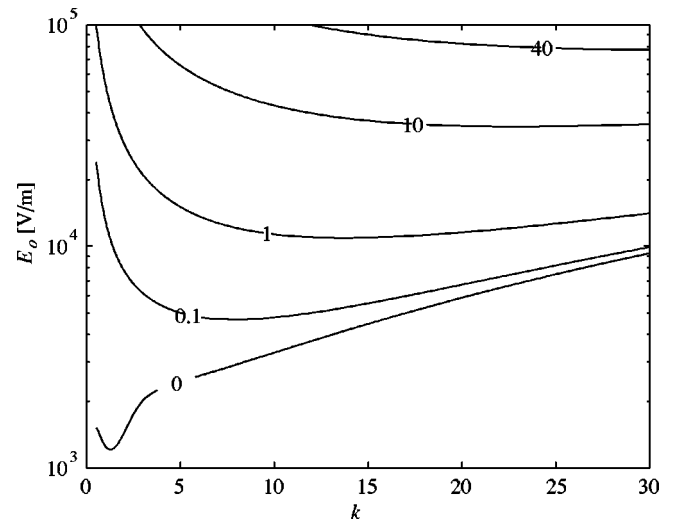

FIG. 3. Contour plot of growth rate as a function of the applied electric field and wave number shown for a conductivity ratio of $\gamma = 1.05$. Contour values are in units of s^{-1}. The critical wave number increases with increasing electric field strength.

field is directed along the streamwise direction. For the remaining base-state variables, $\bar{u} = -(1/R_v)(d\bar{\phi}/dx)$, and $d\bar{\phi}/dx = -1$. The linearized set of disturbance equations for the stiff system are

$$\xi^2 \, \mathrm{Re}(s\hat{\omega} + ik\bar{u}\hat{\omega}) = \xi^2 \nabla_h^2 \hat{\omega} - 3\hat{\omega} + \frac{d\bar{\phi}}{dx}\frac{\partial \hat{\rho}_e}{\partial y}, \tag{62}$$

$$\nabla_h^2 \hat{\psi} + \hat{\omega} = 0, \tag{63}$$

$$\nabla_h^2 \hat{\phi} = -\hat{\rho}_e, \tag{64}$$

$$\mathrm{Pe}_j\left(s\hat{c}_j + ik\bar{u}\hat{c}_j - ik\frac{d\bar{c}_j}{dy}\hat{\psi}\right)$$
$$= \nabla_h^2 \hat{c}_j + \chi_j\left(\bar{c}_j \nabla_h^2 \hat{\phi} + \frac{d\bar{c}_j}{dy}\frac{\partial \hat{\phi}}{\partial y} + ik\frac{d\bar{\phi}}{dx}\hat{c}_j\right), \tag{65}$$

$$\hat{\rho}_e = \frac{F}{\rho_{e,o}}\sum_j c_{j,o}z_j\hat{c}_j. \tag{66}$$

Dirichlet boundary conditions were implemented for the disturbance streamfunction along with homogeneous Neumann boundary conditions for the disturbance potential and concentration,

$$\hat{\psi}_{y=\pm 1} = 0, \tag{67}$$

$$\left.\frac{\partial \hat{\phi}}{\partial y}\right|_{y=\pm 1} = 0, \tag{68}$$

$$\left.\frac{\partial \hat{c}_j}{\partial y}\right|_{y=\pm 1} = 0. \tag{69}$$

The slip and stress-free conditions for the perturbation variables become

$$\left.\frac{\partial \hat{\psi}}{\partial y}\right|_{y=\pm 1} = -\frac{ik}{R_v}\hat{\phi} \tag{70}$$

and

$$\hat{\omega}_{y=\pm 1} = 0. \tag{71}$$

We solved the system using a pseudospectral (collocation) method.[23,24] Eigenvalue convergence was obtained using 36 points and confirmed using a 72 point expansion. This system is found to be linearly unstable for our parameter range of interest. Figure 3 shows a contour plot of growth rate as a function of wave number. Unless otherwise specified, the base-state conductivity ratio was 1.05, the arithmetic mean conductivity of the two streams was 25 μS/cm, and the diffuse interface was roughly 410 μm wide. Other parameter values can be found in Table I. The slip boundary condition [Eq. (70)] was used unless otherwise noted. Typical eigenmodes for some of the disturbance variables are

TABLE I. Table of geometric and material parameters used in the linear stability analysis and nonlinear simulations (unless otherwise noted).

Symbol	Description	Value
a	Channel half-width	$0.5E-3$ m
b	Channel half depth	$0.5E-4$ m
ρ	Density	$1E3$ kg/m^3
μ	Absolute viscosity	$1E-3$ kg/m s
ϵ	Permittivity	$6.9E-10$ C/V m
ζ	Zeta potential	$-8.0E-2$ V
T	Absolute temperature	300 K
z_j	Ion valence number $\{A^+,B^-,K^+,Cl^-\}$	$\{+1, -1, +1, -1\}$
κ_j	Ion diffusivity $\{A^+,B^-,K^+,Cl^-\}$	$\{8E-11, 8E-11, 2E-9, 2E-9\}$ m^2/s

$$[\hat{\psi}(y)]\,exp\,(ikx)$$

$$[\hat{\rho}_e(y)]\,exp\,(ikx)$$

$$[\hat{c}_{A^+}(y)+\hat{c}_{B^-}(y)]exp\,(ikx)$$

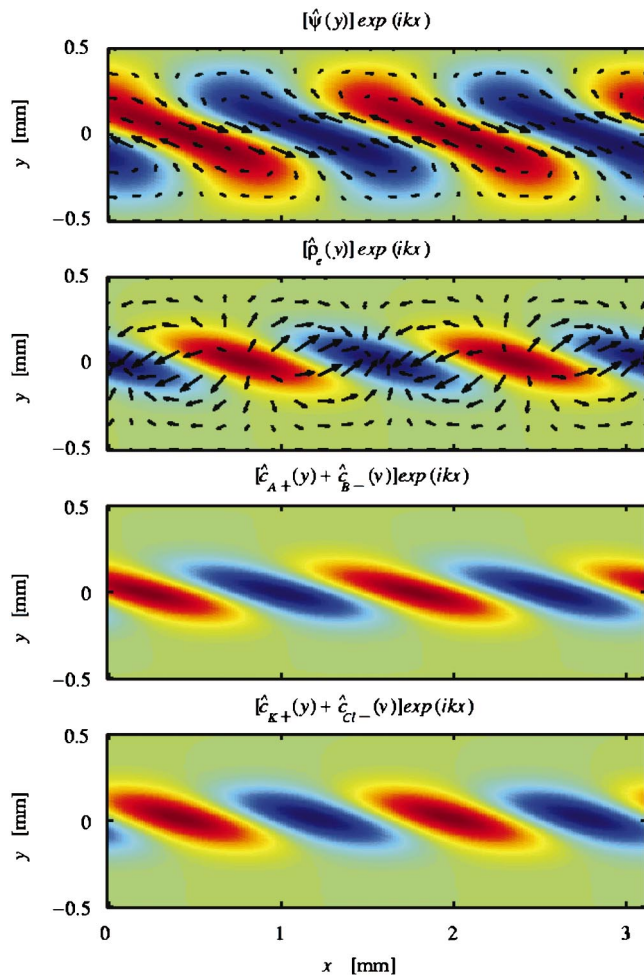$$[\hat{c}_{K^+}(y)+\hat{c}_{Cl^-}(y)]exp\,(ikx)$$

FIG. 4. (Color). Pseudocolor plots of typical eigenfunctions obtained from the linear stability analysis, shown here for $\gamma=1.05$ and $k=2$. Superposed on the streamfunction and charge density plots are the respective disturbance velocity and electric fields.

shown in Fig. 4. Superposed on the disturbance streamfunction and charge density plots are the disturbance velocity and electric field components, respectively.

Next, we discuss various aspects of the model. We begin by considering the differences between the current four-ion model versus the simpler SBE two-ion model. Growth rate contours as a function of applied field and wave number are plotted in Fig. 5 for the four-ion model and for two versions of the two-ion model (using either K^+ and Cl^- or A^+ and B^- as binary mixtures). The two-ion AB model simply neglects the presence of KCl and uses the initial AB ion distribution shown in Fig. 3. The two-ion KCl model neglects the presence of the AB ions and assumes an initial distribution for KCl similar to that of the AB ions shown in Fig. 3. First, either of the two-ion models clearly predicts more stable behavior than the four ion model. The highly asymmetric nature of the AB and KCl, four-ion electrolyte (and its associated spatial gradients in ion mobility) clearly has a destabilizing influence over symmetric binary electrolyte systems. This is, for example, in contrast to the systems considered by Lin *et al.*[10] and Chen *et al.*,[9] where the conductivity field was dominated by a single pair of ions with ap-
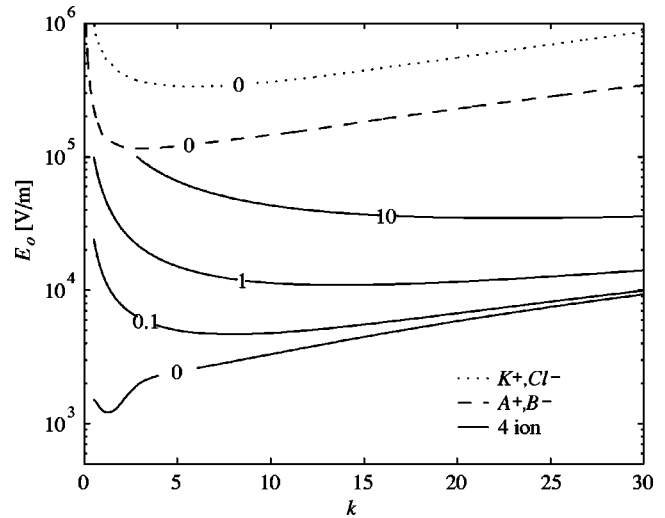
FIG. 5. Contour plot of growth rate as a function of applied electric field and wave number for the two-ion and four-ion models. The dotted and dashed lines show two-ion model results for $\{K^+, Cl^-\}$ and $\{A^+, B^-\}$ binary electrolyte systems, respectively. The solid line shows results for the four-ion model $\{A^+, B^-, K^+, Cl^-\}$. The four-ion model predicts a critical field strength approximately two orders of magnitude lower than either of the simple two-ion models.

proximately equal mobilities. Second, the curves show that the two-ion system is more stable for increased diffusivity (i.e., as the diffusivity is changed from that of KCl to AB). This trend is in agreement with the observation that diffusion is a stabilizing effect while advection is destabilizing.[7] Third, in comparison to the two-ion models, the four-ion model exhibits significant growth rates at an applied electric field strength approximately two orders of magnitude lower than the two-ion models. Lastly, the critical wave numbers for the low-range $s_R=0.1\ s^{-1}$ growth rate are approximately the same for all models.
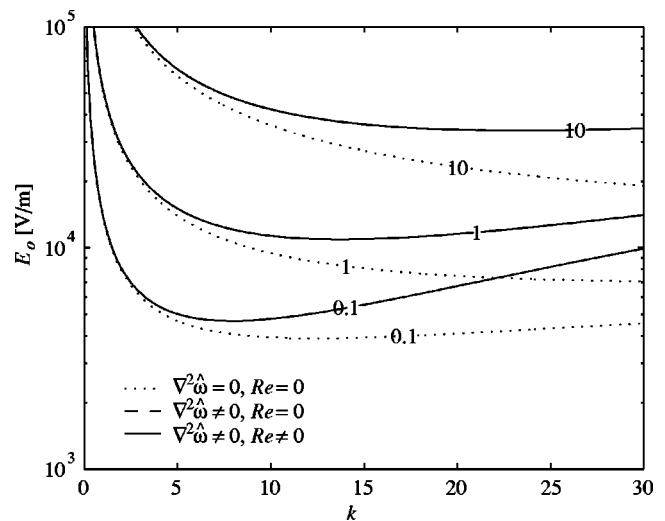
FIG. 6. Growth rate contours as a function of applied electric field and wave number for the three cases: viscous stress and inertial terms neglected ($\nabla_h^2\hat{\omega}=0$, Re$=0$, dotted line), viscous stress term retained and inertial term neglected ($\nabla_h^2\hat{\omega}\neq0$, Re$=0$, dashed line), both viscous stress and inertial terms retained ($\nabla_h^2\hat{\omega}\neq0$, Re$\neq0$, solid line).
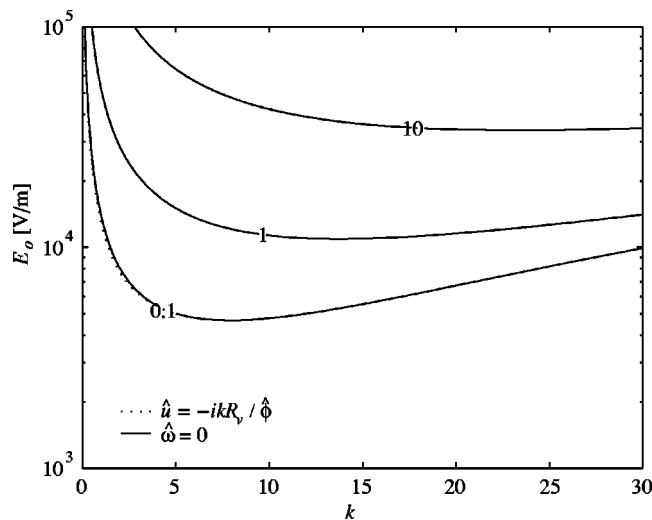
FIG. 7. Growth rate contour plot as a function of applied electric field and wave number for either slip [Eq. (65)] or stress-free [Eq. (66)] boundary conditions. The growth rate contours coincide nearly identically, indicating a negligible difference between the boundary conditions.
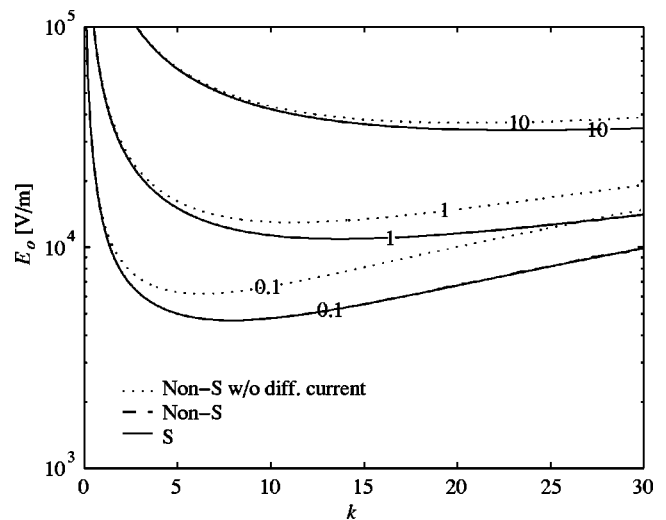
FIG. 8. Growth rate contours shown as a function of applied electric field and wave number, shown for the nonstiff with diffusion current neglected (dotted), nonstiff with diffusion current (Non-S, dashed), and stiff (S, solid) equation sets. Including the diffusion current in the nonstiff equation set results in growth rates that coincide with those of the stiff equation set. By comparison, excluding the diffusion current term in the nonstiff equation set introduces error for high wave number disturbances.

We next explore the influence of the inertial and viscous stress terms [first terms on the left- and right-hand sides of Eq. (62), respectively] in the momentum/vorticity equations. Figure 6 shows several growth rate contours as a function of applied electric field and wave number for three cases: $\nabla_h^2\hat{\omega}=0$, Re$=0$ (viscous stress-free and inertia-free), $\nabla_h^2\hat{\omega} \neq 0$, Re$=0$ (viscous stress and inertia-free), $\nabla_h^2\hat{\omega} \neq 0$, Re $\neq 0$ (viscous stress and inertia). In $\nabla_h^2\hat{\omega}=0$, Re$=0$, both viscous stress and inertia terms were neglected, while in the $\nabla_h^2\hat{\omega} \neq 0$, Re$=0$ case the viscous stress term was retained and the inertial term neglected. Both the viscous stress and inertial terms were retained in the $\nabla_h^2\hat{\omega} \neq 0$, Re $\neq 0$ case. We note from Fig. 6 that the growth rate contours associated with $\nabla_h^2\hat{\omega} \neq 0$, Re$=0$ and $\nabla_h^2\hat{\omega} \neq 0$, Re $\neq 0$ coincide, indicating that the inertial term has negligible influence on the stability of the system for our parameter range of interest. We also note that for high wave numbers, neglecting the viscous stress term ($\nabla_h^2\hat{\omega}=0$, Re$=0$) results in a lower applied field strength necessary for a given growth rate (relative to the $\nabla_h^2\hat{\omega} \neq 0$, Re$=0$ and $\nabla_h^2\hat{\omega} \neq 0$, Re $\neq 0$ cases). The viscous stress term exhibits a stabilizing influence on the high wave number disturbances. The Laplacian associated with the viscous stress term may be viewed as a mode-dependent smoothing operator, which has negligible influence on low wave number disturbances, but significantly damps high-frequency fluctuations of the velocity field.

In Fig. 7, we explore the influence of the slip [Eq. (70)] versus stress-free [Eq. (71)] boundary conditions on the LSA. The growth rate contours associated with the slip and stress-free contours are observed to overlap for the parameter regime shown. This indicates that both boundary conditions have the same influence on the linear instability dynamics.

We now explore any differences between the stiff versus nonstiff system of equations. Figure 8 displays growth rate contours for the following three cases: nonstiff system of equations, neglecting diffusion current, Non-S (nonstiff system with diffusion current), and S (stiff system of equations).

First, note that the contour associated with the nonstiff set without diffusive current deviates from the coinciding contours of the Non-S and S cases, particularly at midrange to high wave numbers. This indicates that retaining the diffusion current term in the nonstiff equation set is vital to accurately capturing the physics associated with the stiff set of equations. Since the diffusion current term is proportional to the Laplacian of the concentration field, high-frequency fluctuations in the concentration field are preferentially damped relative to disturbances characterized by large wavelengths. This discrepancy, however, diminishes as the applied electric field increases, since the ratio of the diffusive current to electromigration current is inversely proportional to E_o.
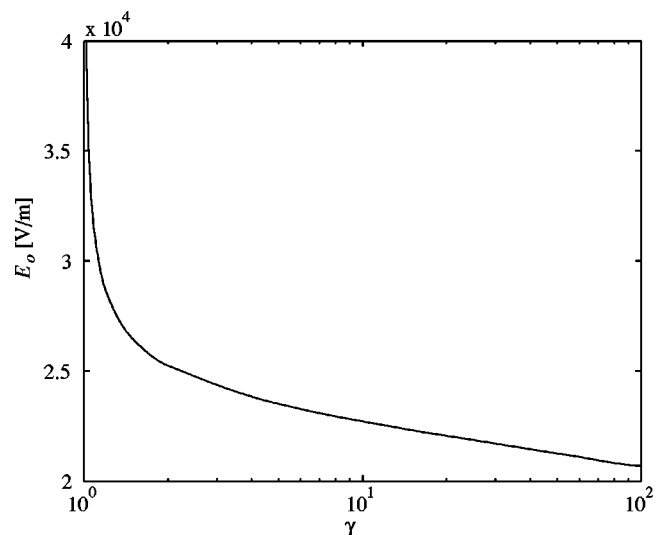
FIG. 9. Critical electric field vs conductivity ratio. Here the critical electric field is defined as the electric field strength associated with a growth rate $s_R=10$ s^{-1} and the critical wave number.
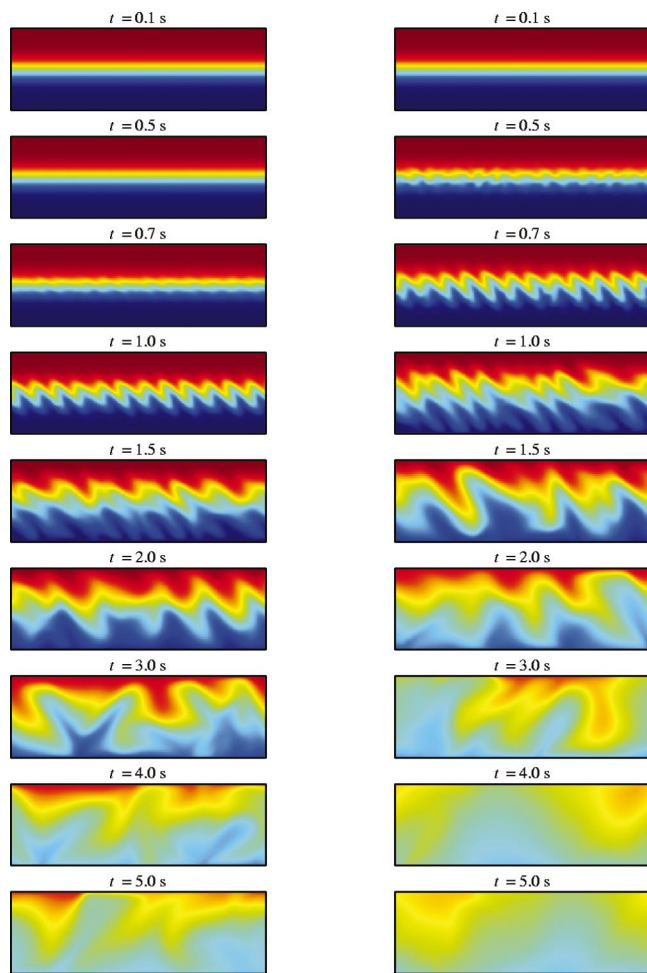
FIG. 10. (Color). Representative image sequence from the nonlinear simulation. The color map is proportional to the summed concentration fields of the A^+ and B^- ions. The left and right columns are the results obtained from applied field strengths of 54.5 and 72.7 kV/m, respectively. Electroosmotic flow is from left to right and the size of the images correspond to physical dimensions of 1×3.1 mm^2. Band-limited white noise with a magnitude of 10^{-6} relative to the initial mean concentration was added to the initial concentration fields. In addition to the white noise, eigenfunctions associated with the $k = 12$ mode were also added to the base state concentration fields, with a relative magnitude of 10^{-6}.
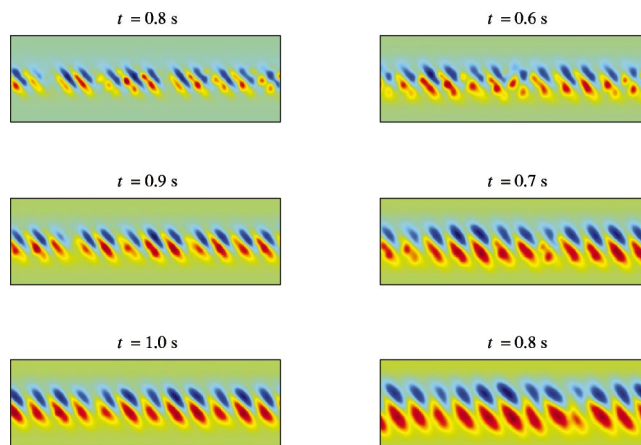

FIG. 11. (Color). Image sequence showing temporal evolution of the predicted disturbance dye field in Fig. 10 (field strengths of 54.5 and 72.7 kV/m for the left and right columns, respectively). The size of each image corresponds to physical dimensions of 1×3.1 mm^2. These disturbance distributions are in good qualitative agreement with the predictions of the linear stability model.

V. TWO-DIMENSIONAL NONLINEAR SIMULATION

We solved the full nonlinear equations, using the Non-S (nonstiff) formulation of Eqs. (32)–(35), (20), and (58). The equations are solved using a pseudo-spectral collocation method.[25,26] The variables were expanded in the spanwise direction using Chebyshev polynomials and a Fourier series in the streamwise direction. Time advancement was accomplished using the second-order Adams–Bashforth/backward differentiation implicit scheme. 64 and 32 points in the streamwise and spanwise directions provided reasonable accuracy and computational time. To insure accuracy and validate the codes, growth rates predicted by the simulation were compared with those predicted by the linear stability analysis results (in all cases, these agreed to within about 4%).

The boundary conditions are periodic and so it is convenient to decompose the electric field into applied and disturbance fields as

$$\mathbf{E} = -\nabla_h \phi = \mathbf{e}_x - \nabla_h \phi_d, \qquad (72)$$

where the variables are shown in nondimensional form. Note that this decomposition slightly modifies Eqs. (32), (34), (35), and (58).

Following the discussion in Fig. 6 above, we chose to neglect the inertial terms in the Navier–Stokes equations, while retaining the in-plane viscous stress term. Similarly, following the discussion in Fig. 7, we implemented a stress-free boundary condition rather than the slip-condition to increase the speed of the computations. Implementation of the slip condition adds additional computational overhead as two boundary conditions are specified for the streamfunction and none for the vorticity. This added complexity can be addressed using an influence matrix technique described by Peyret[25] (again, at the expense of some additional computation).

Figure 10 shows predictions of the evolution of the dye concentration field for two different applied field strengths. The color map in each region corresponds to the summed

Figure 9 displays the dependence of the critical electric field as a function of γ. Here the critical electric field is defined as the electric field strength associated with a growth rate of 10 s^{-1} and the critical wave number (a definition which aids comparisons with experiment, as near-neutral stability behavior is difficult to quantify experimentally). As the conductivity ratio increases, the critical field decreases, with the critical field exhibiting strong dependence at low-conductivity ratios and a weaker dependence at higher ratios.

Regarding the conductivity profile, we note that the linear stability of the system depends only on the conductivity ratio rather than the mean conductivity. Lastly, we observe that the growth rate contours in Figs. 3 and 5–9 are independent of the value of wall ζ potential, provided that the ζ potential is uniform (or nearly so). Note that the low-conductivity ratio values of interest here result in nearly uniform ζ potentials. Changes in the absolute value of ζ potential influence only the phase speed of the disturbances.

concentration of the A^+ and B^- ions, $c_{A^+}(\mathbf{x},t)+c_{B^-}(\mathbf{x},t)$. Dark red corresponds to the maximum summed concentration, while dark blue is a minimum summed concentration of 0 mol m^{-3}. The initial conditions of these simulations were the same as those of the base state of the linear stability analysis. To initialize the disturbance, band-limited white noise was added to the concentration distributions. The maximum amplitude of the white noise did not exceed 10^{-6} times the mean value of each base-state concentration field. Note that even machine round-off error is enough to eventually lead to instability.

For a zero base-state electroosmotic flow, the unstable modes predicted by the LSA are symmetric complex conjugates (i.e., $s_{1,2}=s_R\pm is_I$), corresponding to either rightward or leftward slanting cells (leftward slanting cells are shown in Fig. 4). Assuming a uniform, nonzero electroosmotic base state, as reported here, simply results in a shift in the phase speed of the disturbance, where the magnitude and direction of the shift is equal to that of the base-state flow field (see Refs. 6 and 10 for further discussion). Seeding the initial condition with only band-limited white noise, results in both leftward and rightward slanting modes, corresponding to the complex conjugates predicted by the LSA, appearing in the simulation. In our experiments, however, only leftward slanting cells appear, as will be presented in Fig. 15. We therefore chose to preferentially excite the leftward slanting mode by superposing a $k=12$ eigenfunction to the band-limited white noise discussed above. This eigenfunction is observed experimentally and near the critical value predicted by the LSA. The magnitude of this seeded $k=12$ mode was again less than 10^{-6} of the mean value of the concentration field.

Initially the $k=12$ mode displays the fastest growth rate. The growth rate for these cases was estimated from the growth of the spanwise velocity component, as $s_R=16.9$ and 26.7 s^{-1}, respectively, for the 54.5 and 72.7 kV/m cases. These growth rate values are in excellent agreement with the linear stability analysis predictions of 16.8 and 25.7 s^{-1} for the $k=12$ mode. This agreement provides strong evidence that the base state can be considered quasi-steady for the time scale of interest. After the initial exponential growth period predicted by the linear analysis, lower modes are excited, eventually leading to nonlinear stirring of the concentration fields. Images of the disturbance dye field shown in Fig. 11 may be compared to the eigenfunctions presented in the linear stability analysis section above. The disturbance dye field is calculated as follows $[c_{A^+}(\mathbf{x},t)+c_{B^-}(\mathbf{x},t)]-[c_{A^+}(\mathbf{x},0)+c_{B^-}(\mathbf{x},0)]$.

VI. EXPERIMENTAL APPARATUS AND METHOD

A. Microchannel setup

Figure 12 shows a schematic of the microchannel setup used in the present experiments. The setup consisted of a borosilicate glass capillary (Wilmad Labglass, Buena, NJ) with a rectangular cross section having inner dimensions of 1 mm$\times$100 μm and a 40 mm length. The capillary wall thickness was 100 μm. Custom-built acrylic manifolds were sealed to the capillary ends using silicone adhesive; these provided robust inlet and outlet ports to the microchannel
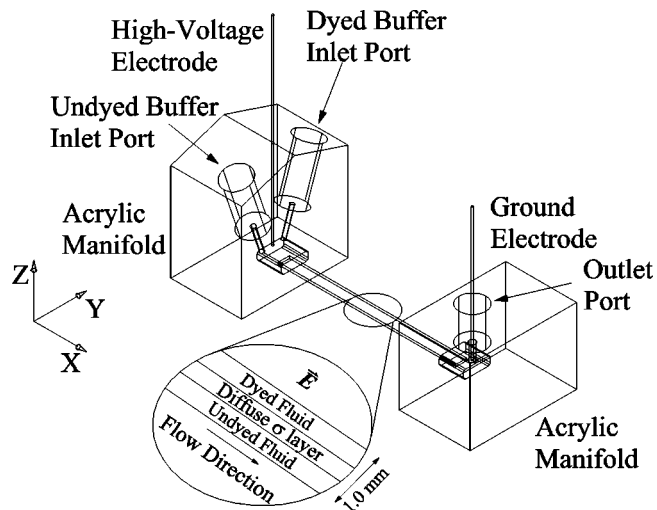

FIG. 12. Schematic of the microchannel setup. The channel is 1 mm wide, 100 μm deep, and 40 mm long. The electrode spacing is 55 mm. Dyed and undyed buffer solutions are introduced at their respective inlet port using a syringe pump. The buffer solutions are advected through the microchannel forming a single stream with a spanwise conductivity gradient. Images were collected at the center of the capillary as shown schematically in the magnified inset.

and housed platinum electrodes. Dyed and undyed buffer solutions pumped through the capillary using a syringe pump (PHD 2000, Harvard Apparatus, MA), completed the electrolytic cell. A 10 mM HEPES buffer (Sigma-Aldrich Corp, MO) solution was used as a background solution to ensure uniform and steady pH. To aid flow visualization, a 2 μM solution of dextran-rhodamine B dye conjugate (Molecular Probes, OR) was added to one of the buffer solutions. This electrically neutral, high-molecular weight (70 kDa) dye was chosen to minimize both electrophoretic drift and molecular diffusion of the dye molecules during the experiments. For the 10 s duration of the experiments, fluctuations of the imaged dye concentration field are therefore predominantly associated with stirring of the background liquid rather than molecular diffusion. To increase the mean value of the flow system's ionic conductivity, the dyed and undyed solutions were doped with equal amounts of potassium chloride. The resulting conductivity ratio between solutions was 1.05$\pm$ 0.15 and the mean conductivity was 25 μS/cm. Current measurements conducted in a measurement cell of known geometry and at low applied voltages (to avoid Joule heating) were used to estimate the ionic conductivity. The measured current was steady and reproducible in these conductivity measurements, suggesting negligible Joule heating influence on the measured conductivity values. Lastly, note that these dilute electrolytes can be assumed to have the permittivity and viscosity of pure water.

B. Imaging and high-voltage system

Dye concentration fields were visualized using the system shown in Fig. 13. The imaging system consisted of an epifluorescent microscope (Nikon TE 300) and a 4$\times$ objective with a numerical aperture of 0.2 and an effective depth of field of 12.5 μm. Illumination provided by a 100 W mer-
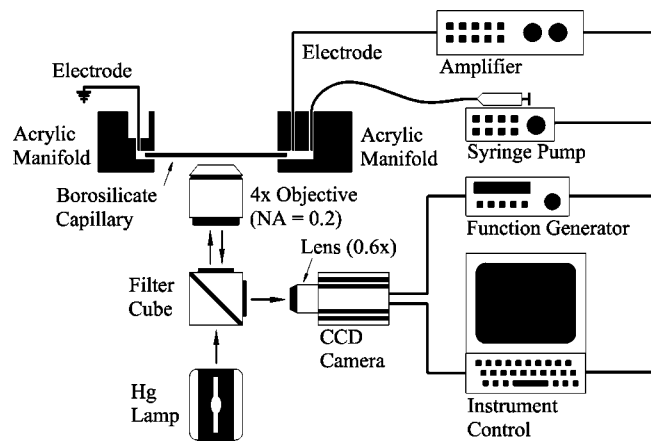
FIG. 13. Schematic of the experimental setup. The fluorescent dye field was imaged using an inverted, epifluorescent microscope and a high-resolution CCD camera. Instrument synchronization was achieved using LABVIEW. A function generator ensured that images were taken at 10 frames per second. The amplifier provided the high-voltage Heaviside signal.

cury lamp was spectrally filtered using an optical filter cube (XF 101-2 Omega Optical, Inc., Brattleboro, VT) with peak absorption and emission wavelengths of 525 and 565 nm, respectively. To increase the field of view, a 0.6× demagnifying lens was included in the optical train, resulting in an overall magnification of 2.4×. Image data were recorded using a charge-coupled device (CCD) camera (CoolSnap fx, Roper Scientific Inc., AZ) with 12 bit intensity resolution. Individual camera pixels were binned to form 4×4 super pixels to increase signal-to-noise ratio and frame rate at the expense of spatial resolution. The final binned dimensions of the super pixels were 26.8×26.8 μm^2 in the image plane. For the present experimental conditions, an exposure time of 15 ms for each frame proved sufficient for using the full dynamic range of the camera. Camera control was achieved using v++ imaging software (Digital Optics Ltd., Auckland, New Zealand), while camera frame rate was held at a constant ten frames per second using a function generator (Agilent 33120a). Large potential differences of order 1–5 kV were applied across the capillary using the high-voltage system shown in Fig. 13. The high-voltage system consisted of a high-voltage amplifier (10/10b, Trek Inc., NJ) controlled using a LABVIEW-controlled DAQ card (National Instruments Inc.).

C. Experimental procedure and image data collection

Prior to the introduction of the buffer solutions into the capillary, a 100 mM sodium hydroxide solution (1.6 ml at 80 μl/min) was flushed through the microchannel to prepare the surface for electroosmotic flow. The NaOH was then flushed from the capillary with deionized water (1.6 ml at 40 μl/min). The syringes on the syringe pump were than loaded with the dyed and undyed buffer solutions and connected to the upstream manifold. Pressure-driven flow caused by the syringe pump resulted in a flow field where dyed and undyed buffer solutions were introduced into the upper and lower halves (of the spanwise or y direction) of the microchannel, respectively.

Apart from the initial capillary setup, the entire data collection procedure was automated using LABVIEW to prevent variation between individual experimental realizations due to operator error. A realization consisted of flushing the capillary with 32 μl of the buffered solutions at a flow rate of 12.8 μl/min. The pump was then deactivated and the solution stream was allowed to diffuse for 90 s. The total time associated with these steps resulted in a diffuse interfacial layer at the axial center of the capillary equal to about 40% of the capillary width. Next, LABVIEW triggered the camera function generator and sent a Heaviside voltage signal to the amplifier. The camera acquired a single frame for each incoming pulse of the 10 Hz pulse train supplied by the function generator. The high-voltage amplifier amplified the Heaviside signal 1000 fold. For all cases, voltage and current were recorded (simultaneously) as images were recorded.

VII. EXPERIMENTAL OBSERVATIONS

Image data

A representative set of images from experiment is shown in Fig. 14 for applied potentials of 3000 and 4000 V. Given the electrode spacing of 55 mm, the applied field strengths are 54.5 and 72.7 kV/m. The potential of the high-voltage electrode was raised nearly instantaneously (<16 μs ramp-up time, as per the slew rate of the amplifier) at $t=0$ s.

Images were corrected using flat and dark field images according to the following formula: CI=OI−DF/FF−DF, where CI, OI, DF, and FF represent the corrected, original, dark-field, and flat-field images, respectively.

The images show an initially diffuse interface that is uniform in the axial direction. Within a second of application of the high voltage, the interface is visibly disturbed and the images show a repeatable spatial fluctuation. The disturbance grows nearly uniformly with time until about 1.5 s, after which the growth rate of the disturbance decreases and structures in the scalar field simply propagate downstream.

VIII. IMAGE ANALYSIS

The diffusive Peclet number of our experiment is on the order of 10^5, so that we may safely assume that rapid fluctuations in the dye concentration field are associated with stirring of the background liquid rather than molecular diffusion. We therefore assume that buckling and stretching of the diffuse interface between the dyed and undyed buffers streams is a direct consequence of spanwise and transverse fluid motions caused by the instability. Images of the disturbance dye field are shown in Fig. 15. The disturbance images were computed from the corrected images as CI(t)−CI(t=0). The characteristic slanted features of the disturbance images are qualitatively very similar to those predicted by the nonlinear simulations described in Sec. V. The initially weak disturbance grows in intensity and in space, eventually spreading to more than half of thes spanwise width of the channel as predicted by the nonlinear model.

Estimates of the critical wave number may be extracted from the experiment images using an isointensity contour
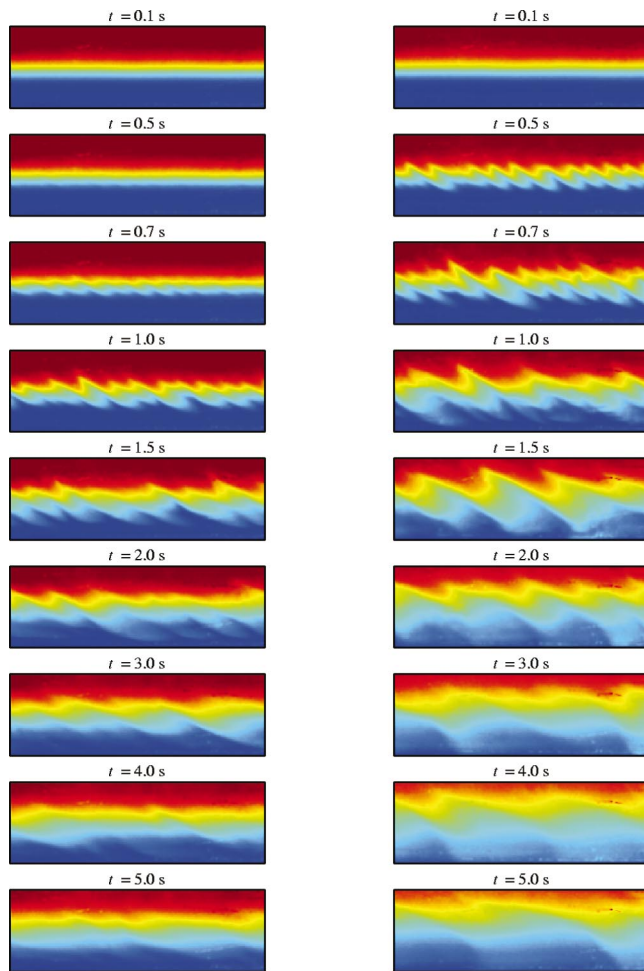
FIG. 14. (Color). Representative images of the fluorescent dye visualization experiments. The left and right columns show results obtained for applied field strengths of 54.5 and 72.7 kV/m, respectively. Image dimensions correspond to 1×3.1 mm^2 in physical space. A pseudocolor map has been used where dark red corresponds to a maximum dye concentration and dark blue corresponds to zero dye concentration. The disturbance in the concentration field initially exhibits a high wave number of ≈ 21.8 mm^{-1} (corresponding to $k=10.9$) for the 54 kV/m case and 23.0 mm^{-1} ($k=11.5$) for the 72 kV/m case. After about 1.5 s, the dominant mode shifts to a lower wave number.
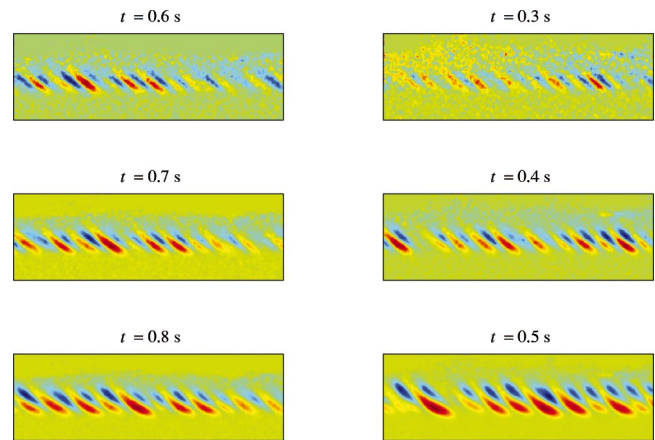

FIG. 15. (Color). Image sequence from experiments showing temporal evolution of the disturbance dye field calculated from corrected images as $CI(t) - CI(t=0)$. Applied field strengths of 54.5 and 72.7 kV/m are shown. Image dimensions are 1×3.1 mm^2. The slanted cellular features of the disturbed dye field are qualitatively very similar to those predicted by the simulations in Fig. 11.

electric fields, as expected. This critical value (predicted by the LSA) can be compared to the maximum measured values of 10.9 ± 0.9 and 11.5 ± 0.8 for the 54.5 and 72.7 kV/m experimental data, respectively. The rapid drop of the critical wave number and subsequent order 4 s decay evidenced in the experiments is well captured by the simulations.

Finally, estimates of the growth rate were obtained from the experimental images by analyzing the temporal growth of the measured intensities associated with the disturbance dye field. Figure 17 shows a plot of the ensemble-averaged disturbance intensity as a function of time for the two ap-
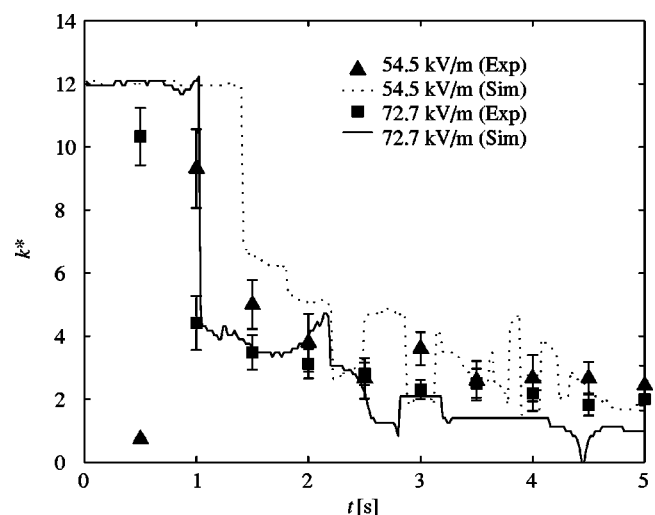
method. This process was achieved as follows. First, high-spatial-frequency image noise was reduced by filtering the image using a Wiener filter. Next, the isointensity contour associated with the maximum spatial variation or amplitude was computed from the filtered image. The power spectrum of this contour was computed along with the power spectra from ten immediately adjacent contours with intensities spaced by a value of 5% of the maximum contour intensity. Prior to computing power spectra, frequency leakage was reduced by multiplying the isointensity contour data with a one-dimensional Hanning window (along the axial direction). The resulting 11 power spectra were than ensemble averaged. The critical wave number was determined directly from the frequency with the largest ensemble-averaged power-spectral density.

The temporal evolution of the critical wave number is shown in Fig. 16 for both the experimental data and simulations. First, for times between $t=0$ and ~ 1 s, the model clearly showed an amplification of the $k=12$ mode for both

FIG. 16. Critical wave number as a function of time for experimental and simulation data using an isointensity contour method. Both experimental and simulation data are shown for two electric field strengths. The experimental data points are shown with error bars corresponding to 95% confidence interval. Each experimental data point represents an ensemble of 9 and 16 realizations for the 54.5 and 72.7 kV/m cases, respectively. The isointensity contour method was also applied to the simulation data. Single realizations are shown for the 54.5 (dashed) and 72.7 (solid) kV/m cases. The simulation data show the same general trends as the experimental data and the absolute values are in fairly good agreement. The initially high wave number disturbances decay into lower frequency modes as time progresses.
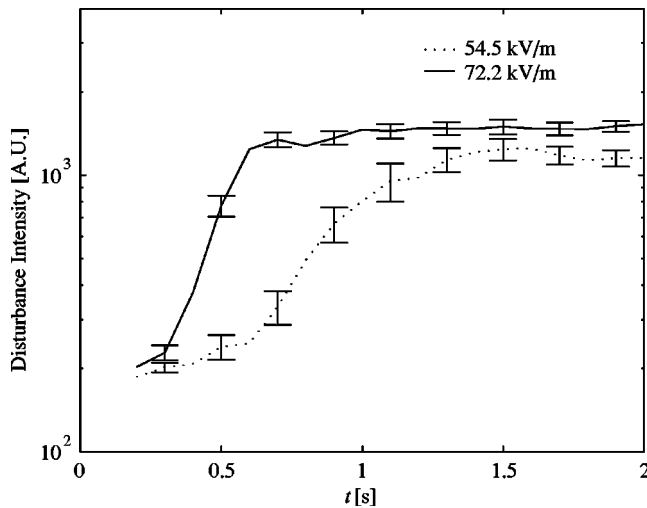
FIG. 17. Measured disturbance intensity as a function of time. The disturbance intensities represent the maximum absolute intensity of the disturbance dye fields. The curves represent ensemble-averaged values with 9 and 16 realizations for the 54.5 and 72.7 kV/m cases, respectively. Errorbars reflect 95% confidence intervals. Growth rates are estimated from the maximum slope of the disturbance intensity.

plied fields. We define the disturbance intensity as the maximum absolute intensity of the disturbance dye field. The initial slope ($t < \sim 1$ s) is roughly linear when plotted on a logarithmic scale, suggesting an exponential dependence as predicted by the model. The slope of the exponential portion of these curves provides an estimate of the growth rate. This slope is $\approx 3.9 \pm 1.9$ and 7.2 ± 1.0 s^{-1} for the 54.5 kV/m and 72.7 kV/m cases, respectively. These values can be compared to the growth rates predicted by the linear stability analysis of 16.8 and 25.7 s^{-1} for the $k=12$ mode. The model clearly overpredicts the initial growth rate by a factor of $\sim 3-4$. The reason for this discrepancy is unclear to us but may be in part due to uncertainties in the diffusivity and mobility of electrolyte ions, and the uncertainty in the conductivity ratio. For example, for the 54.5 and 72.7 kV/m cases and a slightly lower conductivity ratio of 1.01, the LSA predicts values of 10.1 and 15.5 s^{-1}, respectively, for the $k=12$ mode. For our experiments, $\gamma = 1.01$ is well within our uncertainty range for the conductivity ratio ($\gamma = 1.05 \pm 0.15$).

IX. PHYSICAL MECHANISM

In this section we address the instability mechanism responsible for the reduced threshold field conditions in the current multiple species model, and compare this with the earlier SBE model.[6,7,9–11] We noted in Sec. IV that the threshold field conditions for the $\gamma = 1.05$ system was reduced by approximately two orders of magnitude for the MSEKI model versus the SBE model. The main difference between the MSEKI and SBE models is the transport of conductivity. The development of the conductivity field in SBE is strictly due to advection and diffusion. In MSEKI, electromigration plays a key role.

We can derive a conductivity transport equation by summing the individual species transport equations Eq. (34) or

$$\frac{D_h \sigma}{Dt} = \sum_j \frac{1}{Pe_j} \nabla_h^2 c_j + \sum_j \frac{\chi_j}{Pe_j} \nabla_h \cdot (c_j \nabla_h \phi). \quad (73)$$

Equation (73) is valid for non-SBE systems or systems consisting of three or more ions or binary systems with asymmetric transport properties. In such systems, electromigration often plays a significant role in the transport of conductivity. Conductivity transport occurs through three mechanisms: advection, diffusion, and electromigration. As a result of electromigration, ions can "stack" or accumulate in regions of conductivity gradient. This stacking generates conductivity gradients greater than the initial condition (base state). This fundamental destabilizing mechanism captured by the MSEKI model accounts for the large deviation in the threshold field conditions between the MSEKI and SBE models.

In contrast to the MSEKI model, a SBE system has unique values for χ and Pe ($\chi_1 = -\chi_2 = \chi$ and $Pe_1 = Pe_2 = Pe$), and the difference of two ions appears explicitly in the third term of Eq. (73) which reduces to $(\chi/Pe)\nabla_h \cdot [(c_2 - c_1)\mathbf{E}]$. Here, the electroneutrality approximation[14,15] results in a symmetry condition of the form $c_1 \approx c_2$ and Eq. (73) reduces to

$$\frac{D_h \sigma}{Dt} = \frac{1}{Pe} \nabla_h^2 \sigma. \quad (74)$$

This simplification is not allowed for systems with three or more ions or binary systems with asymmetric transport properties. For such systems, the electroneutrality approximation implies that $\Sigma_j z_j c_j \approx 0$. This net neutrality approximation may be met by, for example, arbitrary values of the ratio c_2/c_1, and the concentration and mobility of all ions must be considered. For example, consider the case of a binary electrolyte with asymmetric mobilities. For such system, the third term of Eq. (73) reduces to $\nabla_h \cdot [(q_2 - q_1)\mathbf{E}]$ where $q_j = |\chi_j| c_j / Pe_j$, and the term $\Sigma_j z_j c_j$ does not explicitly appear.

As shown in Eq. (74), conductivity in a SBE system evolves due to bulk liquid advection and diffusion alone, and increases of conductivity gradient above the initial condition can be neglected. LSA results with and without the electromigration terms confirm the negligible influence of electromigration in governing conductivity transport in SBE systems (in accordance with the electroneutrality assumption).

We now present a brief review of the accumulation of charge mechanism common to both the MSEKI and SBE models. We begin by considering a perturbed conductivity field comprises high- and low-conductivity electrolyte streams occupying distinct half-widths of a channel as shown in Fig. 18 (at the top and bottom half of each schematic, respectively). As a result of an externally applied electric field $\mathbf{E}$, charge accumulates near the interface of the high- and low-conductivity regions. The ion density responsible for the charge density, ρ_e is small compared to background ions and net positive where $\nabla_h \sigma \cdot \mathbf{E} < 0$ and net negative where $\nabla_h \sigma \cdot \mathbf{E} > 0$. Charge accumulation is a direct consequence of current conservation, from which the following expression may be derived: $\rho_e = -(\nabla_h \sigma / \sigma) \cdot \mathbf{E}$ (in the absence of ion diffusion).
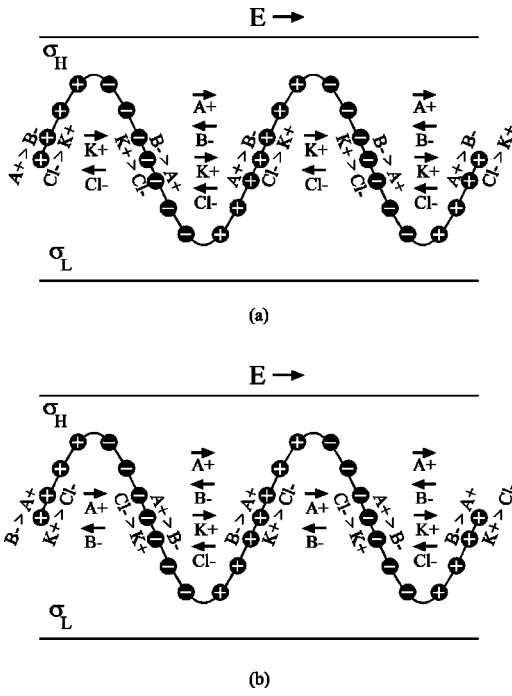
FIG. 18. Schematics of perturbed conductivity fields, net charge distribution, and direction of ion migration shown for two cases. (a) High-conductivity region containing A^+, B^-, K^+, and Cl^- ions and low-conductivity region containing only K^+ and Cl^- ions. The concentration of KCl is initially uniform throughout the system and the conductivity gradient is formed by A^+ and B^- ions. This configuration results in stacking of the conductivity field. (b) High conductivity containing K^+, Cl^-, A^+, and B^- ions and a low-conductivity region containing only A^+ and B^- ions. The concentration of AB is initially uniform and the conductivity gradient is formed by K^+ and Cl^- ions. Here the initial configuration results in destacking of the conductivity field.

Next, we discuss the role of ion accumulation in four-ion MSEKI systems. We will consider the case where AB ions have a mobility much smaller than those of KCl ions, but the general principles discussed here apply to all multi-ion systems. For a general multi-ion system, we can directly express the flux of ion conductivity due to electromigration as

$$\mathbf{J}_{\sigma,em} = \sum_j \frac{\chi_j}{Pe_j} c_j \mathbf{E}. \tag{75}$$

For our four-ion system, Eq. (75) becomes

$$\mathbf{J}_{\sigma,em} \approx \frac{|\chi|}{Pe_{KCl}} (c_{K^+} - c_{Cl^-}) \mathbf{E}. \tag{76}$$

The transport terms associated with A^+ and B^- ions are negligible because of their much lower mobility. The direction of conductivity transport due to electromigration is therefore largely dictated by the sign of $(c_{K^+} - c_{Cl^-})\mathbf{E}$.

Whether electromigration is destabilizing or not depends on the ion configuration. In Fig. 18, we present two four-ion systems which result in opposite signs of $(c_{K^+} - c_{Cl^-})\mathbf{E}$ within the low-conductivity region. Figure 18(a) is a destabilizing case, while Fig. 18(b) is a stabilizing case. For the system of Fig. 18(a), A^+ and K^+ ions in the high-conductivity region electromigrate in the direction of the applied electric field and accumulate in the region of net positive charge. Conversely, B^- and Cl^- ions starting in the high-conductivity region electromigrate in the opposite direction and accumulate in the region with net negative charge. A similar segregation of ions occurs with the K^+ and Cl^- ions that start in the low-conductivity region. These net charge regions then generate a disturbance electric field $\mathbf{E}'$ directed from regions of net positive to net negative charge. The result of both the perturbed and applied fields is that the local flux of K^+ ions exceeds that of the Cl^- ions into regions of $\rho_e < 0$, resulting in a region where $(c_{K^+} - c_{Cl^-}) > 0$. For regions of $\rho_e > 0$, $(c_{Cl^-} - c_{K^+}) > 0$. As per Eq. (76), this results in a net transport of conductivity from regions of low conductivity into regions of high perturbed conductivity. This results in a net increase of local conductivity gradients (referred to here as "conductivity stacking") and can represent a significant destabilizing mechanism.

In the system of Fig. 18(b), electromigration leads to lower conductivity gradients and stabilization. Here the KCl forms the conductivity gradient ions and the AB complex forms the background ions. In this configuration, $(c_{Cl^-} - c_{K^+}) > 0$ for regions of $\rho_e < 0$ and $(c_{K^+} - c_{Cl^-}) > 0$ for regions of $\rho_e > 0$. As per Eq. (76), this electromigration is now responsible for "destacking" the conductivity field. In other words, the conductivity of regions of perturbed high-conductivity decrease, while the conductivity of low-conductivity regions increase. Electromigration, in this instance, enhances ion dispersion and is stabilizing (similar to diffusion).

We can further demonstrate the stabilizing or destabilizing influence of electromigration in the MSEKI model by

TABLE II. Table of required conductivity ratio γ for conditions of $E_o = 3.91E4$ V/m, $k = 12$, Re = 0, such that the growth rate is $s_R = 10.0$ s^{-1}.

Case	Ions	$\nabla\sigma$ ions	Conductivity ratio γ	Terms neglected
1	A^+ and B^-	A^+ and B^-	48.0	None
2	A^+, B^-, K^+, and Cl^-	A^+ and B^-	1.05	None
3	K^+ and Cl^-	K^+ and Cl^-	71.0	None
4	K^+, Cl^-, A^+, and B^-	K^+ and Cl^-	120.0	None
5	A^+, B^-, K^+, and Cl^-	A^+ and B^-	48.0	Electromigration
6	K^+, Cl^-, A^+, and B^-	K^+ and Cl^-	71.0	Electromigration

considering several symmetric and asymmetric ion systems. Table II shows the critical influence of electromigration on instability dynamics. Six cases involving the A^+, B^-, K^+, and Cl^- ions are considered. The second and third columns list the ions considered and the conductivity-gradient-forming ions, respectively. So-called "background" ions are initially present in uniform concentration, while "conductivity-gradient-forming ions" have an initial sharp spanwise conductivity gradient. The fourth column lists the necessary spanwise conductivity gradient as predicted by a LSA analysis to achieve a growth rate of $s_R = 10.0$ s^{-1} for an electric field strength $E_o = 3.91E4$ V/m, wave number of $k = 12$, and Re$= 0$. The fifth column lists any terms that were neglected in the species conservation equation or Eq. (34).

For the two-ion SBE system composed of A^+, B^- ions (case 1), and $\gamma = 48$. However, for the same system with KCl added as a background electrolyte (case 2), γ sharply decreases to 1.05. This is a direct result of stacking of the conductivity field due to electromigration as per the discussion above. The stabilizing influence of destacking of the conductivity field is seen in case 3. In this case, a SBE of KCl ions results in $\gamma = 71$; as compared to KCl with added AB background ions (case 4) where γ increases to 120. The latter four-ion case is a stabilizing, conductivity destacking situation.

We further note the importance of electromigration in cases 5 and 6. In these last two calculations, electromigration terms are neglected in the four-ion case system. The values of γ required for instability correspond to those of the respective SBE cases (based on the conductivity-gradient-forming ions). For these last two, oversimplified (i.e., incorrect) cases, background ions bear no influence on instability, and stability is determined solely by conductivity-gradient-forming ions.

Lastly, we show calculations of the ion concentration fields, including the effects of electromigration stacking of conductivity. Figure 19 shows a plot of the relative increase or decrease of the conductivity ratio as a function of time as predicted by nonlinear simulations for cases 1–4 listed in Table II. As expected the conductivity ratio increases with time for case 2 and decreases for case 4. The conductivity ratio also decreases for cases 1 and 3, but at a slower rate as compared with case 4, due to the enhanced diffusion effect of the destacking present.

X. CONCLUSIONS

The potential advantages associated with using microfluidic devices to perform bioanalytical techniques are well documented and have earned these devices significant attention since the early 1990s. Many of these devices use applied electric fields to leverage electroosmosis and electrophoresis for sample flow control and separation of ionic species. The exact chemistry of samples in these systems is often unknown or poorly characterized, resulting in electrical conductivity mismatches between the sample and the background buffer or electrolyte. These conductivity gradients in the presence of applied electric fields can lead to electrokinetic instabilities which create significant sample dispersion.
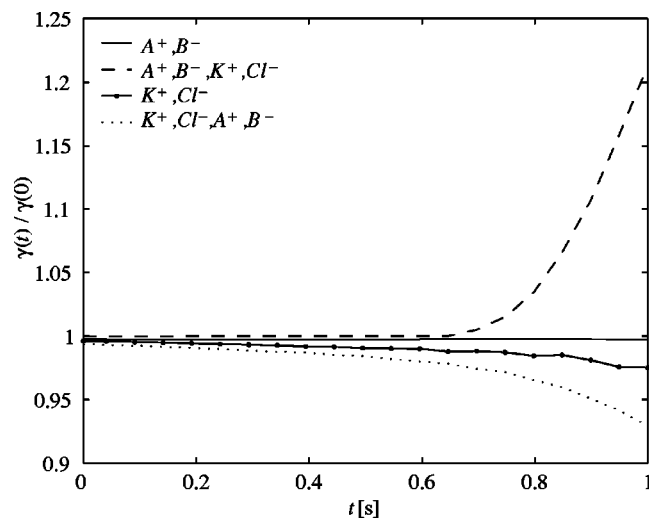

FIG. 19. Normalized conductivity ratio as a function of time for cases 1–4 of Table II. Here $\gamma(t)$ denotes the maximum conductivity of the field divided by the minimum conductivity at any time t. The first two ions listed in the legend correspond to the conductivity-gradient-forming ions. For the four-ion cases, the last two ions are the background ions and have an initially uniform concentration throughout the channel. As expected, the conductivity ratio decreases for the A^+ and B^- case (case 1) and the K^+ and Cl^- case (case 3). For the A^+, B^-, K^+, and Cl^- case (case 2), the conductivity ratio increases as a result of stacking due to electromigration. For the K^+, Cl^-, A^+, and B^- case (case 4), the conductivity ratio decreases at a faster rate than case 3, due to the enhanced ion dispersion caused by destacking of the conductivity field.

We have developed a multiple-species model for predicting the onset and dynamics of electrokinetically driven flow instability. This more general MSEKI model relaxes the common assumption of a symmetric, binary electrolyte, allowing a theoretically arbitrary number of ions with differing thermophysical properties to be considered. This model retains terms in the species conservation equations associated with the electromigration of individual species and allows for EKI studies involving multiple species with differing thermophysical properties such as diffusivity and mobility.

The MSEKI model captures the significant influence of electromigration on the transport of conductivity and the instability dynamics of non-SBE systems (i.e., systems consisting of three or more ions or binary systems with asymmetric transport properties). Unlike SBE systems, where conductivity transport occurs through advection and diffusion alone, in non-SBE systems the transport of conductivity occurs through advection, diffusion, and electromigration of charged species. As a result of electromigration, ions can either stack or destack causing conductivity gradients larger than the initial condition (base state), thereby exerting either a destabilizing or stabilizing influence, respectively. This fundamental instability mechanism captured by the MSEKI model accounts for the large deviation between the threshold conditions predicted by the MSEKI and SBE models. For instance, comparisons between LSA results using the MSEKI model and the SBE models (for the case of $\gamma = 1.05$) show an onset of instability occurring at field strengths nearly two orders of magnitude lower for the MSEKI model, which is in good agreement with the low-conductivity ratio, multi-ion experiments presented here. The

LSA results demonstrate that even in the presence of slight conductivity gradients, ion stacking resulting from electromigration can lead to instabilities in multi-ion electrokinetic systems.

The multi-ion MSEKI model reported here is important in cases where the ions which largely determine the base-state conductivity gradient are highly asymmetric with respect to the background ions; hence violating the SBE assumptions. This is the case explored here where background ions were simple KCl ions, but the gradient was solely determined by large, low mobility *AB* dye ions. This asymmetry leads to localized conductivity stacking and ultimately results in reduced threshold conditions as compared with SBE systems. For cases where KCl ions determine both background conductivity and the conductivity gradient, the two-ion and multi-ion models provide similar results.

Other contributions of the MSEKI model include the development of a nonstiff version of the original stiff equation set to aid numerical simulation of EKI. In this nonstiff set, we show that ionic current due to molecular diffusion represents an important component. We also show through the LSA results of the depth-averaged governing equations that retaining the in-plane viscous stress term in the conservation of momentum is important for damping of high wave number disturbances, despite being second order in the asymptotic expansion. The linear stability analysis also shows that inertia plays a negligible role and that EKI dynamics are insensitive to whether an electrokinetic slip or stress-free boundary condition is enforced.

Full nonlinear simulations of the governing equations show good qualitative and quantitative agreement with experiments. The features and dynamics of the disturbance dye field observed in experiments are well captured by simulation, as well as the temporal evolution of the critical wave number. Growth rates extracted from the experimental images are within a factor of 3–4 of those predicted by simulation and LSA. We expect this discrepancy may be in part due to the uncertainty associated with the measurement of the conductivity ratio and the limitations of the four-ion chemistry model. The model should be useful in the design and optimization of multi-ion electrokinetic systems.

ACKNOWLEDGMENTS

[1] P. A. Auroux, D. Iossifidis, D. R. Reyes, and A. Manz, "Micro total analysis systems. 2. Analytical standard operations and applications," Anal. Chem. **74**, 2637 (2002).

[2] A. Manz, N. Graber, and H. M. Widmer, "Miniaturized total chemical-analysis systems—a novel concept for chemical sensing," Sens. Actuators B **1**, 244 (1990).

[3] J. M. Ramsey, S. C. Jacobson, and M. R. Knapp, "Microfabricated chemical measurements systems," Nat. Med. **1**, 1093 (1995).

[4] A. van den Berg and T. S. J. Lammerink, "Micro total analysis systems: Microfluidic aspects, integration concept and applications," Microsystem Technology in Chemistry and Life Science **194**, 21 (1998).

[5] J. R. Melcher and G. I. Taylor, "Electrohydrodynamics—a review of role of interfacial shear stresses," Annu. Rev. Fluid Mech. **1**, 111 (1969).

[6] J. F. Hoburg and J. R. Melcher, "Internal electrohydrodynamic instability and mixing of fluids with orthogonal field and conductivity gradients," J. Fluid Mech. **73**, 333 (1976).

[7] J. C. Baygents and F. Baldessari, "Electrohydrodynamic instability in a thin fluid layer with an electrical conductivity gradient," Phys. Fluids **10**, 301 (1998).

[8] M. H. Oddy, J. G. Santiago, and J. C. Mikkelsen, "Electrokinetic instability micromixing," Anal. Chem. **73**, 5822 (2001).

[9] C-H. Chen, H. Lin, S. K. Lele, and J. G. Santiago, "Convective and absolute electrokinetic instability with conductivity gradients," J. Fluid Mech. **524**, 263 (2005).

[10] H. Lin, B. D. Storey, M. H. Oddy, C. H. Chen, and J. G. Santiago, "Instability of electrokinetic microchannel flows with conductivity gradients," Phys. Fluids **16**, 1922 (2004).

[11] B. D. Storey, B. S. Tilley, H. Lin, and J. G. Santiago, "Electrokinetic instabilities in thin microchannels," Phys. Fluids **17**, 018103 (2005).

[12] L. D. Landau and E. M. Lifshitz, *Electrodynamics of Continuous Media*, Course of Theoretical Physics Vol. 8, 2nd ed. (Pergamon, Oxford, 1984).

[13] *Electrohydrodynamics*, edited by A. Castellanos (Springer, Vienna, 1998).

[14] V. L. Levich, *Physicochemical Hydrodynamics* (Prentice-Hall, Englewood Cliffs, NJ, 1962).

[15] R. F. Probstein, *Physicochemical Hydrodynamics*, 2nd ed. (Wiley, New York, 1994).

[16] P. J. Scales, F. Grieser, T. W. Healy, L. R. White, and D. Y. C. Chan, "Electrokinetics of the silica solution interface—a flat-plate streaming potential study," Langmuir **8**, 965 (1992).

[17] S. H. Yao, D. E. Hertzog, S. L. Zeng, J. C. Mikkelsen, and J. G. Santiago, "Porous glass electroosmotic pumps: Design and experiments," J. Colloid Interface Sci. **268**, 143 (2003).

[18] H. Lin, B. D. Storey, and J. G. Santiago, "A depth-averaged model for electrokinetic flows in a thin microchannel geometry," *Proceedings of the International Mechanical Engineering Conference and Exposition*, Anaheim, CA, 13–19 November 2004 (American Society of Mechanical Engineers, New York, 2004), Vol. IMECE2004-61017.

[19] P. Moin, *Fundamentals of Engineering Numerical Analysis* (Cambridge University Press, Cambridge, 2001).

[20] Molecular Probes, Inc. Handbook of Fluorescent Probes and Research Products, 2003. Dextran Conjugates; http://www.probes.com/media/pis/mp01800.pdf

[21] P. G. Drazin and W. H. Reid, *Hydrodynamic Stability* (Cambridge University Press, Cambridge, 1982).

[22] A. J. Bard and L. R. Faulkner, *Electrochemical Methods: Fundamentals and Applications*, 2nd ed. (Wiley, New York, 2001).

[23] L. N. Trefethen, *Spectral Methods in Matlab* (Society for Industrial and Applied Mathematics, Philadelphia, 2000).

[24] J. A. C. Weideman and S. C. Reddy, "A matlab differentiation matrix suite," ACM Trans. Math. Softw. **26**, 465 (2000).

[25] R. Peyret, *Spectral Methods For Incompressible Viscous Flow*, Applied Mathematical Sciences Vol. 148 (Springer, Berlin, 2002).

[26] J. P. Boyd, *Chebyshev and Fourier Spectral Methods*, 2nd ed. (Dover, New York, 2001).